

Integrating Secure and High-Speed Communications into Frequency Hopping MIMO Radar

Kai Wu, J. Andrew Zhang, *Senior Member, IEEE*, Xiaojing Huang, *Senior Member, IEEE*, and Y. Jay Guo, *Fellow, IEEE*

Abstract—Dual-function radar-communication (DFRC) based on frequency hopping (FH) MIMO radar (FH-MIMO DFRC) achieves symbol rate much higher than radar pulse repetition frequency. Such DFRC, however, is prone to eavesdropping due to the spatially uniform illumination of FH-MIMO radar. How to enhance the physical layer security of FH-MIMO DFRC is vital yet unsolved. In this paper, we reveal the potential of using permutations of hopping frequencies to achieve secure and high-speed FH-MIMO DFRC. Detecting permutations at a communication user is challenging due to the dependence on spatial angle. We propose a series of baseband waveform processing methods which address the challenge specifically for the legitimate user (Bob) and meanwhile scrambles constellations almost omnidirectionally. We discover a deterministic sign rule from the signals processed by the proposed methods. Based on the rule, we develop accurate algorithms for information decoding at Bob. Confirmed by simulation, our design achieves substantially high physical layer security for FH-MIMO DFRC, improves decoding performance compared with existing designs and reduces mutual interference among radar targets.

Index Terms—DFRC, FH-MIMO radar, physical layer security, hopping frequency permutation

I. INTRODUCTION

There have been increasing demands for systems with joint communications and radar sensing capabilities, on vehicular platforms such as unmanned aerial vehicles and smart cars [1]. Performing the two functions on one platform by sharing hardware and signal processing modules can achieve immediate benefits of reduced cost, size, weight, and better spectral efficiency [2]. As pointed out in [3], co-designing joint communication and radar sensing can maximize spectral efficiency with the two sub-systems benefiting each other. Targeting at co-design, some researchers optimize dual-function waveform by jointly considering communication and radar sensing performance metrics (e.g., mutual information and achievable rate etc.), leading to an inherent performance trade-off between the two sub-systems [4]–[6]. Some researchers exploit the ubiquitous wireless communication technologies, e.g., IEEE 802.11p [7], IEEE 802.11ad [8]–[10] and mobile communication network [11], to perform radar sensing. These design [4]–[12], however, can have constrained radar sensing ability, as compared with using dedicated radar waveforms.

Integrating secondary data communications in existing radar waveform/platforms, referred to as dual-function radar-communication (DFRC) [13], [14], puts radar sensing first.

MIMO radar has gained popularity in DFRC given its degrees of freedom in both angle and waveform domains [15]–[19]. Conventional modulations, such as phase shift keying (PSK) and amplitude shift keying, are performed in [15], [16] using the sidelobes of beam pattern. Non-traditional modulations, such as waveform shuffling [17] and code shift keying [18], have also been developed by optimizing MIMO radar waveform. These works [15]–[18] generally embed one symbol per one or multiple radar pulses; hence the communication symbol rate is limited by the pulse repetition frequency (PRF).

Employing frequency-hopping (FH) based MIMO (FH-MIMO) radar can increase the symbol rate to much higher than radar PRF, since information embedding can be performed on basis of fast-time sub-pulse [20]–[22]. Hereafter, we refer to FH-MIMO radar-based DFRC as *FH-MIMO DFRC*. In [20], [21], PSK-based FH-MIMO DFRC is developed by adding PSK phases onto FH-MIMO radar waveform. In [22], different combinations of hopping frequencies are used as constellation points and selected per radar hop (aka sub-pulse within a radar pulse) based on information bits to be transmitted, hence referred to as hopping frequency combination selection (HFCS). HFCS decoding can be readily performed by identifying hopping frequencies in the frequency domain. As illustrated in [22], HFCS greatly increases the data rate of FH-MIMO DFRC compared with PSK [21].

However, HFCS-based FH-MIMO DFRC has a low physical layer security which can hinder its effective application. FH-MIMO radar radiates signals uniformly in the spatial region of interest [23]. Thus, any user covered by radar illumination, albeit the angle-of-departure (AoD) with respect to (w.r.t.) radar, can correctly identify hopping frequencies to eavesdrop HFCS bits. The detection probability of hopping frequencies is independent of AoD given the same signal-to-noise ratio (SNR) (which will be detailed in Section II-C). In fact, eavesdropper (Eve), generally having high receiver gain and sensitivity [24], can correctly identify the hopping frequencies with a higher probability compared with a legitimate user.

On the other hand, solely using HFCS has not fully exploited the information embedding capability of hopping frequencies. Given any M hopping frequencies, there are $M!$ number of permutations, each providing a unique pairing between hopping frequencies and antennas. Thus, in addition to HFCS [22], performing hopping frequency permutation selection (HFPS) at radar and detecting HFPS have the potential of boosting the data rate of FH-MIMO DFRC. Unlike HFCS relying on amplitude/power to identify hopping frequencies, HFPS decoding needs to extract signal phases to estimate

K. Wu, J. A. Zhang, X. Huang and Y. J. Guo are with the Global Big Data Technologies Centre, University of Technology Sydney, Sydney, NSW 2007, Australia (e-mail: kai.wu@uts.edu.au; andrew.zhang@uts.edu.au; xiaojing.huang@uts.edu.au; jay.guo@uts.edu.au).

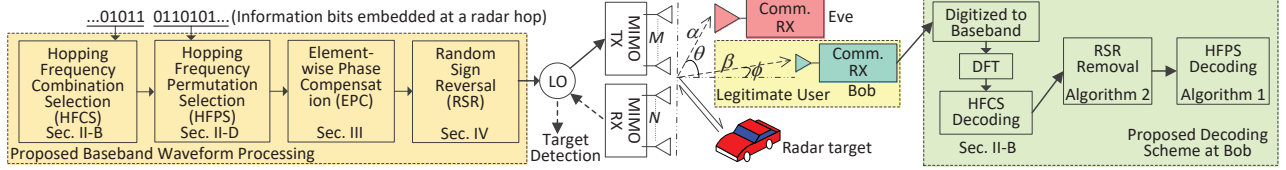


Fig. 1. System block diagram of an FH-MIMO DFRC, where radar, besides detecting targets, also performs downlink communication through an LoS link with a legitimate user named Bob. Meanwhile, there is an unintended user Eve who eavesdrops on the communication between radar and Bob. The proposed baseband waveform processing highlighted on the left ensures a secure communication by scrambling constellations omnidirectionally. The proposed decoding scheme, as highlighted on the right, can recover constellations at Bob to achieve high-speed data communications.

hopping frequency permutation. This poses a challenging AoD-dependent issue, as will be detailed in Section III-A.

In this paper, we design new baseband waveform processing to jointly perform HFCS and HFPS in FH-MIMO DFRC, achieving secure and high-speed data communications solely between radar and legitimate user (Bob). We reveal that, besides improving data rate, using HFPS has the substantial potential of enhancing physical layer security for FH-MIMO DFRC. Our key contributions are summarized as follows.

- 1) Through formulating HFPS decoding problem, we analyze the AoD-dependent issue and accordingly propose an element-wise phase compensation (EPC), removing the AoD dependence of HFPS decoding specifically for Bob. EPC poses a new challenge to Eve by incapacitating HFPS decoding at Eve if not knowing the AoD of Bob;
- 2) Considering the possible acquisition of the AoD of Bob by Eve, we propose a random sign reversal (RSR) processing which scrambles constellations almost omnidirectionally. We prove that RSR can force the symbol error rate (SER) of Eve into converging to one asymptotically;
- 3) We discover a deterministic rule related to the signs and phases of the signals processed by EPC and RSR. Based on the rule, we develop an algorithm for Bob to accurately detect and remove RSR. Enabled by EPC, we also design an algorithm for Bob to efficiently decode HFPS.

We provide a detailed numerical example to demonstrate the overall workflow of incorporating the proposed design in an FH-MIMO DFRC system. We also provide extensive simulations, showing that our design achieves a substantially high communication secrecy and an improved SER performance compared with previous works. As also revealed in simulation, the proposed design suppresses sidelobe spikes in the range ambiguity function of FH-MIMO radar, which hence greatly improves signal-to-interference ratio (SIR) of radar detection.

Notations: The following notations are used throughout the paper. C_M^K denotes binomial coefficient and $M!$ denotes M factorial. $\lfloor \cdot \rfloor$ rounds towards negative infinity. $(\cdot)^T$ takes transpose and $(\cdot)^*$ takes conjugate. $\|\cdot\|_2$ denotes ℓ_2 -norm. $[\cdot]_x$ takes element x of a vector and $[\cdot]_{x,y}$ takes an element from a matrix at row x and column y . \odot denotes elementwise product. $\Re\{x\}$ take the real part of x . $\mathbb{P}\{x = x_0\}$ gives the probability of a random variable x taking x_0 . $\mathbb{E}\{\cdot\}$ takes expectation. $\text{erfc}\{\cdot\}$ denotes the complementary error function. $\mathbf{1}_x$ is an x -dimensional unit vector and $\mathbf{0}_{x \times y}$ denotes an $x \times y$ matrix of zeros.

II. SIGNAL MODELS AND SUMMARY OF OUR DESIGN

In this section, the system structure and signal model of FH-MIMO DFRC are presented. Fig. 1 illustrates the overall system block diagram. The system consists of an FH-MIMO radar, a single-antenna communication user called Bob and a potential eavesdropper called Eve. The radar is equipped with co-located uniform linear arrays as transmitter and receiver. In addition to target detection, the radar also performs downlink data transmission to Bob through an line-of-sight (LoS) channel. In this paper, we focus on developing information embedding and decoding schemes to realize secure and high-speed communications between radar and Bob. Thus, we assume that the channel parameters of Bob are available at radar. Also, we consider a practical scenario that the channel information of Eve is unknown to either radar or Bob.

A. FH-MIMO Radar

Assume that the radar has M transmitter antennas and N receiver antennas. Each radar pulse is divided into H sub-pulses, i.e., hops. Each hop has the time duration of T . The radar frequency band with bandwidth B is divided evenly into K sub-bands. The k -th ($k = 0, 1, \dots, K-1$) sub-band has the baseband central frequency kB/K . At hop h and antenna m , the FH-MIMO radar-transmitted signal is

$$s_{hm}(t) = e^{j2\pi \frac{k_{hm}B}{K}t}, \quad 0 \leq t - hT \leq T, \quad (1)$$

where k_{hm} is the index of the sub-band selected for antenna m at hop h . To ensure waveform orthogonality, the following constraints are imposed on radar parameters [20], [22], [25]

$$k_{hm} \neq k_{hm'} \quad \forall m \neq m', \quad BT/K = r (\geq 1), \quad (2)$$

where r denotes a constant integer.

B. Signal Model of Bob

Denote the AoD of the LoS path between radar and Bob as ϕ and the complex channel gain of the path as β . Each hop of signals received at Bob are sampled into L digital samples by the sampling frequency of $2B$. Based on (1), the i -th baseband signal sample received at Bob is given by

$$y_h(i) = \beta \sum_{m=0}^{M-1} e^{-jmu_\phi} e^{j2\pi r i k_{hm}/L} + \xi(i), \quad (3)$$

where $u_\phi = \frac{2\pi d \sin \phi}{\lambda}$ is referred to as *beam-space AoD* and $\xi(i)$ is additive white Gaussian noise (AWGN). Here, d is the

antenna spacing of the radar transmitter array and λ is the radar wavelength. Taking the L -point DFT of $y_h(i)$, the result at the l -th discrete frequency is

$$Y_h(l) = \beta \sum_{m=0}^{M-1} e^{-jmu\phi} \delta(l - rk_{hm}) + \Xi(l) \quad (4)$$

where $\delta(l)$ is the Dirac delta function and $\Xi(l)$ is the DFT of $\xi(i)$, i.e., $\Xi(l) = \frac{1}{L} \sum_{i=0}^{L-1} \xi(i) e^{j\frac{2\pi li}{L}} \forall l$. See Appendix A for the intermediate calculations of (4).

According to the waveform orthogonality imposed by (2), there are M different hopping frequencies per hop, which leads to M non-zero values of the Dirac delta function in (4). Therefore, by detecting M peaks in $|Y_h(l)|$, the hopping frequencies used at hop h can be identified. Let l_m^* ($m = 0, 1, \dots, M-1$) denote the index of the m -th peak of $|Y_h(l)|$, satisfying

$$l_0^* < l_1^* < \dots < l_{M-1}^*. \quad (5)$$

The M hopping frequencies corresponding to the M peaks can be collected by the following set \mathcal{K}_h ,

$$\mathcal{K}_h = \{l_0^*/r, l_1^*/r, \dots, l_{M-1}^*/r\}. \quad (6)$$

Note that \mathcal{K}_h is a combination of taking M out of K hopping frequencies. The combinations are used as constellation points in [22], where the hopping frequencies per hop are selected at radar based on information bits; and by detecting \mathcal{K}_h at communication receiver, information is decoded.

C. Signal Model of Eve

As FH-MIMO radar transmits signals omnidirectionally, Eve can receive and process radar signals as Bob does. Consider that Eve also takes an L -point DFT per hop. Let θ denote the AoD of Eve, α the channel gain and $X_h(l)$ the DFT result at the l -th discrete frequency. With reference to (3) and (4), we can express $X_h(l)$ as

$$X_h(l) = \alpha \sum_{m=0}^{M-1} e^{-jmu\theta} \delta(l - rk_{hm}) + Z(l), \quad (7)$$

where $u_\theta = \frac{2\pi d \sin \theta}{\lambda}$ denotes the beamspace AoD of the LoS path between radar and Eve, and $Z(l)$ is AWGN at Eve.

Comparing (4) and (7), we see that the Dirac delta function takes non-zero values at the same discrete frequencies, i.e., at $l_m^* \forall m$ given in (5). Without noise, the amplitudes of non-zero $|Y_h(l)|$ and $|X_h(l)|$ are $|\beta|$ and $|\alpha|$, respectively. Clearly, the power of useful signals received at Bob and Eve are independent of their LoS AoDs w.r.t. radar. That is, \mathcal{K}_h can be readily identified at Eve as described in Section II-B for Bob. In fact, due to potentially larger antenna gain [24], Eve can have a higher detection probability of \mathcal{K}_h , compared with Bob. This elaborates the low physical layer security of solely using \mathcal{K}_h for FH-MIMO DFRC, as pointed out in Section I.

D. Overall Description of Proposed Methods

To achieve a secure and high-speed FH-MIMO DFRC, we propose new baseband waveform processing, as illustrated in Fig. 1. There are four modules in the proposed processing, including HFCS, HFPS, EPC and RSR. Below, we illustrate the first two in details, and then provide the motivations of developing the remaining two modules (which will be presented in subsequent sections).

Besides combinations of hopping frequencies, we also use the permutation of hopping frequencies to convey information bits. Referring to Fig. 1, we divide each communication symbol into two sub-symbols. One is used for HFCS which selects one out of C_K^M combinations of hopping frequencies for a radar hop. Given M hopping frequencies there are $M!$ permutations of the frequencies, each providing a pairing between hopping frequencies and antennas. Thus, we use the second sub-symbol to perform HFPS.

A straightforward benefit of introducing HFPS is the increased data rate given the large number of permutations. Given M antennas and K sub-bands, the number of information bits can be conveyed by HFCS and HFPS are up to $\lfloor \log_2 C_M^K \rfloor$ and $\lfloor \log_2 (M!) \rfloor$, respectively. Taking $K = 20$ and $M = 12$ for example, we have $\lfloor \log_2 C_M^K \rfloor = 16$ and $\lfloor \log_2 (M!) \rfloor = 28$. That is, combining HFCS with HFPS can transmit 28 more bits per radar hop than solely using HFCS as designed in [22].

However, this potential of HFPS is non-trivial to fulfill, due to a challenging AoD-dependent issue in decoding HFPS, as will be illustrated in Section III-A. To solve the issue, we devise an EPC processing, based on which an algorithm is designed for Bob to efficiently decode HFPS sub-symbol. This will be elaborated on in Section III-B. Due to EPC, HFPS decoding at Eve relies on not only her own AoD but also that of Bob. Therefore, combining HFPS and EPC can potentially enhance the physical layer security of FH-MIMO DFRC, particularly when Eve does not know the AoD of Bob. This will be unveiled in Section III-C.

Considering that a powerful Eve can manage to acquire the AoD of Bob, the secrecy enhanced by EPC is then limited. To address this issue, we further propose RSR processing on radar baseband waveform, which severely scrambles constellations almost omnidirectionally. The enhanced secrecy protection against Eve is analyzed in Section IV-A. Through investigating the phase changes of the signals processed by EPC and RSR, we discover a deterministic rule to detect and remove RSR for Bob. This will be presented in Section IV-B. In addition, the impact of all the proposed designs on radar detection will be analyzed in Section IV-C. An exemplary FH-MIMO DFRC integrating our design will be presented in Section V.

III. ELEMENT-WISE PHASE COMPENSATION

In this section, the proposed EPC is presented. Through the elaboration of the AoD-dependent issue in HFPS decoding, we develop EPC processing. Then, the potential of using EPC to enhance physical layer security is unveiled.

A. AoD-Dependence Issue of HFPS Decoding

To show the AoD dependence of detecting HFPS, i.e., \mathbf{k}_h , we first formulate the detection problem. By multiplying $Y_h(l)$ given in (4) with β^* , the remaining exponential term $e^{-jmu\phi}$ attached to the l_m^* -th peak is the m -th element of the following steering vector

$$\mathbf{a}_\phi = [1, e^{-ju\phi}, \dots, e^{-j(M-1)u\phi}]^T. \quad (8)$$

Stacking the L peaks of $Y_h(l)$ into a vector, we have

$$\mathbf{y}_h = [Y_h(l_0^*), Y_h(l_1^*), \dots, Y_h(l_{M-1}^*)]^T.$$

Based on (4) and (5), we see that \mathbf{y}_h is a permutation of the β -scaled \mathbf{a}_ϕ , i.e.,

$$\mathbf{y}_h = \beta \mathbf{P}_h \mathbf{a}_\phi + \mathbf{v}, \quad (9)$$

where \mathbf{P}_h is permutation matrix and \mathbf{v} collects M independent noises $\Xi(l_m^*) \forall m$. Multiplying \mathbf{P}_h^T to both sides of (9) gives

$$\mathbf{P}_h^T \mathbf{y}_h = \beta \mathbf{P}_h^T \mathbf{P}_h \mathbf{a}_\phi + \mathbf{P}_h^T \mathbf{v} = \beta \mathbf{a}_\phi + \mathbf{P}_h^T \mathbf{v}, \quad (10)$$

where $\mathbf{P}_h^T \mathbf{P}_h = \mathbf{I}$ is due to the orthogonal property of a permutation matrix. By comparing the two sides of (10) in a pointwise manner, the hopping frequencies attached to the M antennas can be expressed as

$$\mathbf{k}_h = \mathbf{P}_h^T [l_0^*/r, l_1^*/r, \dots, l_{M-1}^*/r]^T. \quad (11)$$

Eq. (11) indicates that HFPS decoding can be performed by identifying the permutation matrix \mathbf{P}_h .

According to (10), the following detector can be formulated to identify \mathbf{P}_h ,

$$\mathbf{P}_h : \min_{\mathbf{P} \in \mathcal{P}} g(\mathbf{P}) \quad \text{s.t.} \quad g(\mathbf{P}) = \|\beta \mathbf{a}_\phi - \mathbf{P}^T \mathbf{y}_h\|_2^2, \quad (12)$$

where \mathcal{P} is the set of possible permutation matrices. From (12), we see that the detecting performance of \mathbf{P}_h varies with the AoD of Bob, i.e., ϕ . This leads to the so-called AoD-dependent issue of HFPS decoding. In particular, given a small ϕ , the distance between adjacent elements in \mathbf{a}_ϕ is also small, leading to a high error probability of detecting \mathbf{P}_h and decoding HFPS. This issue can be relieved with a large ϕ . However, a large ϕ can lead to an ambiguity issue. When $u\phi > \frac{2\pi}{M}$, it can happen that the phases of $e^{-jmu\phi}$ at two or more different values of m are identical.

B. EPC and HFPS Decoding at Bob

We see from (8) the elements of \mathbf{a}_ϕ are similar to the constellation points of the M -PSK modulation. Thus, when $e^{-jmu\phi} \forall m$ are uniformly distributed on the unit circle, the best detecting performance can be achieved [17]. In light of this, we introduce EPC to compensate the phase of each antenna-transmitted signal so that \mathbf{a}_ϕ given in (8) becomes the following AoD-independent steering vector

$$\mathbf{a} = [1, e^{-j2\pi/M}, \dots, e^{-j2\pi(M-1)/M}]^T. \quad (13)$$

Based on (1), (3) and (4), the following EPC is introduced for the m -th antenna at hop h ,

$$\tilde{s}_{hm} = s_{hm}(t) e^{-jm(2\pi/M - u\phi)}. \quad (14)$$

Algorithm 1 HFPS Decoding at Bob

- 1: **Input:** $\tilde{\mathbf{y}}_h, \beta, l_m^* (\forall m)$ and r (given in (2));
 - 2: Take the element angles of $\beta^* \tilde{\mathbf{y}}_h$, and stack them $\tilde{\omega}$;
 - 3: At $\forall m$, if $[\tilde{\omega}]_m > 0$, $[\tilde{\omega}]_m = [\tilde{\omega}]_m - 2\pi$;
 - 4: Sorting the elements of $\tilde{\omega}$ in descending order gives \mathbf{i} ;
 - 5: If $\|e^{j[\tilde{\omega}]_{[i]M-1}} - 1\|_2 < \|e^{j[\tilde{\omega}]_{[i]0}} - 1\|_2$, shift \mathbf{i} circularly by a single element; ▷ Similar to ‘‘circshift()’’ in MATLAB;
 - 6: Substitute \mathbf{i} into (15) to construct \mathbf{P}_h ;
 - 7: Substituting \mathbf{P}_h, l_m^* and r into (11) leads to \mathbf{k}_h ;
 - 8: Look up \mathbf{k}_h in the constellation set to decode HFPS.
-

We add a tilde sign above the relevant variables to reflect the impact of EPC. That is, $y_h(l), Y_h(l), \mathbf{y}_h$ and $g(\mathbf{P})$, as given in (3), (4), (9) and (12), respectively, are now denoted by $\tilde{y}_h(l), \tilde{Y}_h(l), \tilde{\mathbf{y}}_h$ and $\tilde{g}(\mathbf{P})$. Note that

- $\tilde{y}_h(l)$ has the same expression as $y_h(l)$ except that $u\phi$ is replaced by $2\pi/M$. The same goes for $\tilde{Y}_h(l)$;
- $\tilde{\mathbf{y}}_h$ replaces \mathbf{a}_ϕ in (9) with \mathbf{a} given in (13). The same permutation matrix is applicable for both $\tilde{\mathbf{y}}_h$ and \mathbf{y}_h , since EPC does not change the indexes of peaks in $\tilde{Y}_h(l)$; refer to Section II-C.

Jointly considering the above changes caused by EPC, the objective function of problem (12) becomes $\tilde{g}(\mathbf{P}) = \|\beta \mathbf{a} - \mathbf{P}^T \tilde{\mathbf{y}}_h\|_2^2$. Expanding the objective function $\tilde{g}(\mathbf{P})$ gives

$$\tilde{g}(\mathbf{P}) = \|\beta \mathbf{a}\|_2^2 + \|\tilde{\mathbf{y}}_h\|_2^2 - 2\Re\{\beta^* \mathbf{a}^H \mathbf{P}^T \tilde{\mathbf{y}}_h\}.$$

We see that minimizing $\tilde{g}(\mathbf{P})$ is equivalent to maximizing $\Re\{\beta^* \mathbf{a}^H \mathbf{P}^T \tilde{\mathbf{y}}_h\}$ w.r.t. \mathbf{P} , as the other two terms are irrelevant to \mathbf{P} . The maximization is achieved when the pointwise phase difference between \mathbf{a} and $\beta^* \mathbf{P}^T \tilde{\mathbf{y}}_h$ is minimized. Due to EPC, the element phases of \mathbf{a} are in descending order for sure. This implies that the correct \mathbf{P} needs to sort the element phases of $\beta^* \mathbf{P}^T \tilde{\mathbf{y}}_h$ in descending order as well. Let the $M \times 1$ vector \mathbf{i} collect the arrangements of the element phases of $\beta^* \tilde{\mathbf{y}}_h$ into the sorted version. We propose the following solution to (12),

$$[\mathbf{P}_h]_{[i]m,m} = 1 \quad (m = 0, 1, \dots, M-1) \quad (15)$$

where \mathbf{P}_h is initialized as $\mathbf{0}_{M \times M}$.

Based on the above analysis, Algorithm 1 is established to decode HFPS at Bob. In Step 2, directly taking the element angles makes the values in $\tilde{\omega}$ fall in the region of $[-\pi, \pi]$. Thus, Step 3 recovers true angles by compensating -2π on elements larger than 0. This is because all the element angles of $\beta^* \tilde{\mathbf{y}}_h$ should be equal to those of \mathbf{a} given in (13) in the absence of noise, and taking angle in Step 2 adds 2π onto any angle smaller than $-\pi$. Corrupted in noises, the phase of $[\beta^* \tilde{\mathbf{y}}_h]_0$ (which is zero without noise) can become a small positive value which will then be revised through Step 3 into a small negative value close to -2π . This phenomenon, known as zigzag [26], turns the largest element angle of $\beta^* \tilde{\mathbf{y}}_h$ into the smallest one. Step 5 is introduced to remove potential zigzag by comparing the Euclidean distances $\|e^{j[\tilde{\omega}]_{[i]M-1}} - 1\|_2$ and $\|e^{j[\tilde{\omega}]_{[i]0}} - 1\|_2$. Based on (11) and (15), Steps 6 and 7 produce \mathbf{k}_h which is finally used for HFPS decoding in Step 8.

C. Enhancing Physical Layer Security by EPC

As the phase compensation of EPC is determined based on the AoD of Bob, the received signal at Eve is still AoD-dependent. To this end, we can conclude that EPC helps enhance the physical layer security of FH-MIMO DFRC. Taking into account EPC in the frequency-domain signal received at Eve, i.e., $X_h(l)$ given in (7), the signal can be rewritten into

$$\tilde{X}_h(l) = \alpha \sum_{m=0}^{M-1} e^{-jm(\frac{2\pi}{M} + u_\theta - u_\phi)} \delta(l - rk_{hm}) + Z(l). \quad (16)$$

Again, we notice that detecting the set of hopping frequencies, i.e., \mathcal{K}_h , at Eve is not affected by AoD. The same set $\{l_m^* \forall m\}$ given in (6) can be identified at Eve as that obtained at Bob. Similar to \mathbf{y}_h given in (9), the following vector can be obtained at Eve,

$$\tilde{\mathbf{x}}_h = [\tilde{X}_h(l_0^*), \tilde{X}_h(l_1^*), \dots, \tilde{X}_h(l_{M-1}^*)]^T. \quad (17)$$

With reference to (10)~(12), the following detector is formulated at Eve to decode HFPS by identifying the permutation matrix \mathbf{P}_h ,

$$\begin{aligned} \mathbf{P}_h : & \min_{\mathbf{P} \in \mathcal{P}_{\text{Eve}}} f(\mathbf{P}) \\ \text{s.t. } & f(\mathbf{P}) = \begin{cases} \|\alpha \mathbf{a}_{\theta\phi} - \mathbf{P}^T \tilde{\mathbf{x}}_h\|_2^2, & \text{if Eve knows } u_\phi \\ \|\alpha \mathbf{a}_\theta - \mathbf{P}^T \tilde{\mathbf{x}}_h\|_2^2, & \text{otherwise} \end{cases}, \end{aligned} \quad (18)$$

where the two steering vectors are

$$\begin{aligned} \mathbf{a}_{\theta\phi} &= [1, e^{-j(\frac{2\pi}{M} + u_\theta - u_\phi)}, \dots, e^{-j(M-1)(\frac{2\pi}{M} + u_\theta - u_\phi)}]^T \text{ and} \\ \mathbf{a}_\theta &= [1, e^{-j(\frac{2\pi}{M} + u_\theta)}, \dots, e^{-j(M-1)(\frac{2\pi}{M} + u_\theta)}]^T. \end{aligned}$$

Note that the same \mathbf{P}_h is required for Eve and Bob to decode HFPS, since \mathbf{P}_h is added at radar as part of the waveform.

From (18), we see that EPC makes decoding HFPS at Eve relies on not only the AoD of Eve u_θ but also that of Bob u_ϕ . If u_ϕ is unknown to Eve, the decoding performance can degrade drastically, since the actual steering vector contained in $\tilde{\mathbf{x}}_h$ is $\mathbf{a}_{\theta\phi}$. A powerful eavesdropper may manage to know u_ϕ , reducing the secrecy enhancement brought by EPC. This can be solved by a new technique proposed below.

IV. RANDOM SIGN REVERSAL

To further enhance the secrecy of FH-MIMO DFRC, we introduce RSR to scramble the constellations received by Eve, even when the AoD of Bob is known to Eve. As indicated by the name, RSR randomly selects several antennas and reverse the signs of signals transmitted by them. Antennas are randomly and independently selected over hops. In this section, we first explain how RSR can scramble constellations received by Eve, and then develop an algorithm for Bob to remove RSR. We also elaborate the impact of all proposed modules on radar performance. *In the following, we add a breve sign above relevant variables to indicate RSR processing, e.g., $\check{s}_{hm}(t)$ corresponding to the EPC-processed $\tilde{s}_{hm}(t)$ given in (14) and the original radar waveform $s_{hm}(t)$ given in (3).*

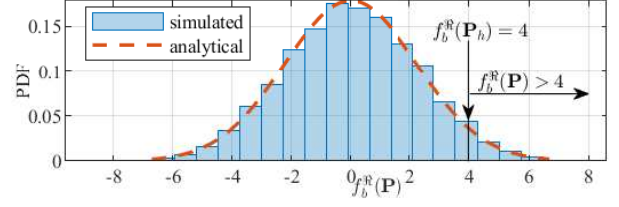


Fig. 2. Histogram of simulated $f_b^{\text{R}}(\mathbf{P})$ and the analytical PDF based on the parameters derived in Proposition 1, where $u_{\theta\phi} = 0$, $M = 8$ and $Q = 2$.

A. Impact of RSR on Eve

We can reflect RSR in radar-transmitted signals by adding a binary coefficient b_{hm} onto $\tilde{s}_{hm}(t)$ given in (14), leading to

$$\check{s}_{hm}(t) = b_{hm} \tilde{s}_{hm}(t) = b_{hm} s_{hm}(t) e^{-jm(2\pi/M - u_\phi)}. \quad (19)$$

Denoting the number of sign-reversed antennas as Q per hop, we have

$$\mathbb{P}\{b_{hm} = 1\} = (M - Q)/M; \quad \mathbb{P}\{b_{hm} = -1\} = Q/M, \quad (20)$$

where \mathbb{P} takes probability. Substituting (19) into (16) and (17), we can rewrite $\check{\mathbf{x}}_h$ into

$$\check{\mathbf{x}}_h = \alpha \mathbf{P}_h (\mathbf{b}_h \odot \mathbf{a}_{\theta\phi}) + \mathbf{z}, \quad (21)$$

where \odot denotes pointwise product and \mathbf{z} collects $Z(l_m^*) \forall m$.

Replacing $\tilde{\mathbf{x}}_h$ in (18) with $\check{\mathbf{x}}_h$, the objective function, denoted by $f_b(\mathbf{P})$ (with the subscript added to reflect the impact of RSR), becomes

$$\begin{aligned} f_b(\mathbf{P}) &= \|\alpha \mathbf{a}_{\theta\phi} - \alpha \mathbf{P}^T \mathbf{P}_h (\mathbf{b}_h \odot \mathbf{a}_{\theta\phi}) - \mathbf{P}^T \mathbf{z}\|_2^2 \\ &= 2M|\alpha|^2 + \tilde{z} - 2|\alpha|^2 \underbrace{\Re\{\mathbf{a}_{\theta\phi}^H \mathbf{P}^T \mathbf{P}_h (\mathbf{b}_h \odot \mathbf{a}_{\theta\phi})\}}_{f_b^{\text{R}}(\mathbf{P})} \end{aligned} \quad (22)$$

where $\|\mathbf{a}_{\theta\phi}\|_2^2 = M$ and $\|\mathbf{P}^T \mathbf{P}_h (\mathbf{b}_h \odot \mathbf{a}_{\theta\phi})\|_2^2 = M$ are plugged in, and \tilde{z} is the sum of noise-related terms. It can be readily confirmed that the variance of \tilde{z} is independent of \mathbf{P} and \mathbf{b}_h . Without RSR, i.e., $\mathbf{b}_h = \mathbf{1}$ in (22), $f_b^{\text{R}}(\mathbf{P})$ is maximized at $\mathbf{P} = \mathbf{P}_h$, which then minimizes $f_b(\mathbf{P})$ without noise. However, affected by RSR, $f_b(\mathbf{P})$ can no longer be maximized at $\mathbf{P} = \mathbf{P}_h$, as detailed in the following.

Proposition 1: *Within the following angular region*

$$0 \leq u_{\theta\phi} \leq \frac{2\pi(M-2)}{M}, \text{ s.t. } u_{\theta\phi} = u_\theta - u_\phi, \quad (23)$$

the proposed RSR makes $f_b^{\text{R}}(\mathbf{P})$ approach a normal distribution with parameters given in (24), which further forces the SER of Eve, who solves (18) for HFPS decoding, into converging to one in high SNR regions.

$$\mu_f = \frac{M-2Q}{M^2} \frac{\sin^2\left(\frac{M(u_{\theta\phi} + \frac{2\pi}{M})}{2}\right)}{\sin^2\left(\frac{(u_{\theta\phi} + \frac{2\pi}{M})}{2}\right)}, \quad \sigma_f^2 = \frac{1}{2}(M - \mu_f^2) \quad (24)$$

Refer to Appendix B for the proof of Proposition 1. Fig. 2 plots the histogram of the simulated $f_b^{\text{R}}(\mathbf{P})$ with the analytical PDF plotted based on the parameters derived in Proposition 1. We see that, as proved, $f_b^{\text{R}}(\mathbf{P})$ conforms to a normal distribution. We also see that the analytical PDF of $f_b^{\text{R}}(\mathbf{P})$ overlaps with the simulated one, which confirms the accuracy

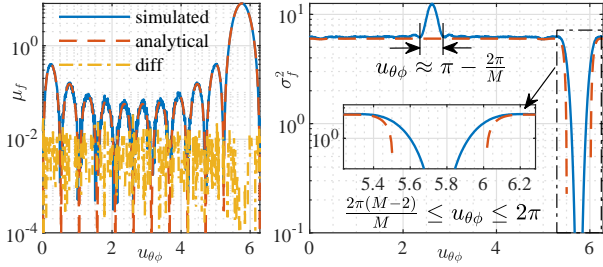


Fig. 3. The mean and variance of $f_b^{\Re}(\mathbf{P})$ vs $u_{\theta\phi}$ with $M = 12$ and $Q = 2$.

of the parameters derived in Proposition 1. Given $M = 8$ and $Q = 2$ in Fig. 2, we have $f_b^{\Re}(\mathbf{P}_h) = 4$. Seen from the figure, there are a non-negligible number of $\mathbf{P} (\neq \mathbf{P}_h)$ leading to $f_b^{\Re}(\mathbf{P}) > f_b^{\Re}(\mathbf{P}_h)$. In this case, solving (18) returns the \mathbf{P} in the region of $f_b^{\Re}(\mathbf{P}) > 4$ (as annotated in Fig. 2) rather than \mathbf{P}_h required by Eve for HFPS decoding.

Fig. 3 compares the simulated and analytical parameters of $f_b^{\Re}(\mathbf{P})$ against $u_{\theta\phi}$. We see that the analytical μ_f given in (24) depicts the mean of $f_b^{\Re}(\mathbf{P})$ accurately over the whole angular region, and the analytical σ_f^2 is accurate for most angles. An exceptional angular region where the analytical and simulated values of σ_f^2 have a non-negligible gap is around $u_{\theta\phi} = \pi - \frac{2\pi}{M}$. In this region, the complex $f_b^{\Re}(\mathbf{P})$ has much smaller imaginary parts (compared with real parts) and even turns into a real value at $u_{\theta\phi} = \pi - \frac{2\pi}{M}$; see (22). Since we take half the variance of $f_b(\mathbf{P})$ as that of its real part $f_b^{\Re}(\mathbf{P})$ (see (37) in Appendix B), the actual variance of $f_b^{\Re}(\mathbf{P})$ is larger than σ_f^2 given in (24) when $u_{\theta\phi}$ is close to $\pi - \frac{2\pi}{M}$ and doubles σ_f^2 at $u_{\theta\phi} = \pi - \frac{2\pi}{M}$. In fact, this exception is favorable to improve communication secrecy. As seen in Fig. 2, a larger variance of $f_b^{\Re}(\mathbf{P})$ increases the number of permutation matrices causing incorrect HFPS decoding at Eve.

Note that, although the region $\frac{2\pi(M-2)}{M} \leq u_{\theta\phi} \leq 2\pi$, denoted by \mathcal{R} , is excluded in Proposition 1; seen from the zoomed-in sub-figure in Fig. 3, the analytical σ_f^2 derived in the proposition can depict the actual variance in part of \mathcal{R} . (The reason for excluding \mathcal{R} is illustrated at the end of Appendix B.) The decoding performance of Eve is low in \mathcal{R} , as explained below. We see from Fig. 3 that \mathcal{R} can be divided into two sub-regions, denoted by \mathcal{R}_1 and \mathcal{R}_2 , with $\sigma_f^2 > 0$ and $\sigma_f^2 \approx 0$, respectively. In \mathcal{R}_1 , since $\sigma_f^2 > 0$, the conclusion in Proposition 1 still holds, i.e., the normally distributed $f_b^{\Re}(\mathbf{P})$ leads to the asymptotic convergence of the SER at Eve. In \mathcal{R}_2 , due to $u_{\theta\phi} + \frac{2\pi}{M} \approx 2\pi$, we have $\mathbf{a}_{\theta\phi} \approx \mathbf{1}_M$, which degrades the decoding performance of Eve and even invalidates (18) at $u_{\theta\phi} + \frac{2\pi}{M} = 2\pi$.

B. Detecting RSR at Bob

Enabled by EPC, Bob can recover RSR-scrambled constellations, which is developed in this subsection. Similar to (21), EPC and RSR turn \mathbf{y}_h given in (9) into

$$\check{\mathbf{y}}_h = \beta \mathbf{P}_h \check{\mathbf{a}} + \mathbf{v}, \text{ s.t. } \check{\mathbf{a}} = (\mathbf{b}_h \odot \mathbf{a}) \quad (25)$$

where \mathbf{a} is given in (13) and \mathbf{v} collects the AWGNs $\Xi(l_m^*) \forall m$ given in (4). We discover a deterministic rule concerning the

Algorithm 2 Removing RSR for Bob

- 1: **Input:** Q , M and $\check{\mathbf{y}}_h$; $\triangleright |\cdot|^2$ takes element-wise absolute square
- 2: Calculate $\mathbf{Y}_h = |\check{\mathbf{y}}_h \mathbf{1}^T - \mathbf{1} \check{\mathbf{y}}_h^T|^2$;
- 3: Identify the minimum element (excluding diagonal element) and its index in each row of \mathbf{Y}_h , stacking them in \mathbf{y}_{\min} and \mathbf{d} , respectively;
- 4: Sort \mathbf{y}_{\min} in ascending order and denote the index vector from \mathbf{y}_{\min} to the sorted version as \mathbf{d}_1 ;
- 5: **for** $q = 0 : Q - 1$ **do** \triangleright Index starts from 0.
- 6: Take $i = [\mathbf{d}_1]_q$ and $i' = [\mathbf{d}]_i$. Remove i' from \mathbf{d}_1 ;
- 7: $[\mathbf{y}_h]_{i^*} = -[\mathbf{y}_h]_{i^*}$, s.t. $i^* = \min_{i,i'} \left\{ \frac{L-l_i^*}{r}, \frac{L-l_{i'}^*}{r} \right\}$;
- 8: **end for**
- 9: **Return** $\tilde{\mathbf{y}}_h = \check{\mathbf{y}}_h$.

element signs and phases of $\check{\mathbf{a}}$ — the joint processing of EPC and RSR turns the m -th element into another one in $\check{\mathbf{a}}$. By assuming $b_{hm} = -1$, $[\check{\mathbf{a}}]_m$ becomes

$$[\check{\mathbf{a}}]_m = -e^{-j\frac{2\pi m}{M}} = e^{j\frac{2\pi M/2}{M}} e^{-j\frac{2\pi m}{M}} = [\check{\mathbf{a}}]_{m \pm \frac{M}{2}}, \quad (26)$$

where $m \pm \frac{M}{2}$ depends on $m \leq \frac{M}{2}$.

The discovered rule enables us to detect RSR by identifying identical elements in $\check{\mathbf{a}}$. However, to ensure correct detection of RSR, two constraints are necessary. *First*, when $b_{hm} = -1$ and $b_{h(m+\frac{M}{2})} = -1$ happen simultaneously, RSR turns $[\check{\mathbf{a}}]_m$ and $[\check{\mathbf{a}}]_{m+\frac{M}{2}}$ into each other. In this case, two reversed antennas will be identified as a single one. To avoid this, we impose the constraint that $b_{hm} = -1$ and $b_{h(m+\frac{M}{2})} = -1$ cannot happen simultaneously, i.e.,

$$b_{hm} + b_{h(m+M/2)} \neq -2 \quad \forall m < M/2. \quad (27)$$

Second, both $b_{hm} = -1$ and $b_{h(m+\frac{M}{2})} = -1$ lead to $[\check{\mathbf{a}}]_m = [\check{\mathbf{a}}]_{m+\frac{M}{2}}$. In turn, $[\check{\mathbf{a}}]_m = [\check{\mathbf{a}}]_{m+\frac{M}{2}}$ can be caused by either $b_{hm} = -1$ or $b_{h(m+\frac{M}{2})} = -1$, incurring ambiguity in RSR detection. To remove the ambiguity, we need to enforce a protocol between radar and Bob that RSR only happens on the antenna associated with smaller (or larger) hopping frequencies. This constraint can be expressed as

$$b_{hm^*} = -1 \text{ s.t. } m^* : \min_{m, m+M/2} \{k_{hm}, k_{h(m+M/2)}\}. \quad (28)$$

Algorithm 2 is designed to remove RSR for Bob based on $\check{\mathbf{y}}_h$ given in (25). In Step 2, the power differences between each element in \mathbf{y}_h and all the other elements are calculated. After Steps 3 and 4, the first several elements in \mathbf{d}_1 are related to the indexes of RSR antennas. In Step 6, the indexes of the two antennas, whose received signals are most similar in power, are extracted. By comparing the associated hopping frequencies, RSR is detected with the aid of constraint (28) and removed by reversing back the sign; see Step 7. It is noteworthy that the removal of RSR at Bob also owes to EPC that only works for Bob (due to the AoD-specific design of EPC). This indicates that Eve cannot remove RSR as Bob does in Algorithm 2.

C. Impact of Proposed Design on Radar Performance

Subsequently, we illustrate the impact of each module in the proposed baseband waveform processing on radar performance

TABLE I
DIFFERENT FH SEQUENCES

	(h, m)	(0, 0)	(0, 1)	(1, 0)	(1, 1)
C1	f_{hm} (MHz)	20	10	45	30
C2	f_{hm} (MHz)	10	20	30	45

TABLE II
COMBINATIONS OF $(\nu, f_{h'm'})$, WHERE THE FREQUENCY IS IN MHZ

(m, m')	(0, 0)	(0, 1)	(1, 0)	(1, 1)
(h, h')	(0, 1)			
$(\nu, f_{h'm'})$, C1	(-20, 30)	(-35, 45)	(-10, 30)	(-25, 45)
$(\tilde{\nu}, \tilde{f}_{h'm'})$, C2	(-25, 45)	(-10, 30)	(-35, 45)	(-20, 30)

using the range ambiguity function. Consider an FH-MIMO radar with M antennas and H hops per pulse. Let τ denote time delay. Based on [25, Eq. (27)], we can express the range ambiguity function of the radar as,

$$R(\tau) = \left| \sum_{m=0}^{M-1} \sum_{m'=0}^{M-1} \sum_{h, h'=0}^{H-1} \underbrace{\chi(\tilde{\tau}, \nu)}_{\mathcal{B}} e^{j2\pi\nu h T} \underbrace{e^{j2\pi f_{h'm'} \tau}}_{\mathcal{D}} \right|, \quad (29)$$

where $\tilde{\tau} = \tau - T(h' - h)$, $\nu = f_{hm} - f_{h'm'}$ and $\chi(x, y)$ is the ambiguity function of a standard rectangular pulse with x and y spanning range and Doppler domains, respectively. According to [25, Eq. (26)], we have

$$\chi(x, y) = \left(T - |x| \right) \mathcal{S} \left(y(T - |x|) \right) e^{j\pi y(x+T)}, \text{ if } |x| < T;$$

and otherwise $\chi(x, y) = 0$, where $\mathcal{S}(\alpha) = \frac{\sin(\pi\alpha)}{\pi\alpha}$. The impact of proposed processing on $R(\tau)$ is analyzed below.

1) *Impact of HFCS on $R(\tau)$* : HFCS selects M out of K different hopping frequency per hop based on varying information bits to be transmitted. The waveform orthogonality condition given in (2) is hence always satisfied under HFCS processing. As conventional FH-MIMO radars randomly selects hopping frequencies [25], HFCS, resembling the random selection, incurs negligible changes to the key features of $R(\tau)$, e.g., mainlobe width and mainlobe-to-sidelobe ratio etc.

2) *Impact of HFPS on $R(\tau)$* : We see from (29) that $R(\tau)$ is determined by the combinations of $(\mathcal{B}, \mathcal{D})$ which is in essence relied on the combinations of $(\nu, f_{h'm'})$. By fixing $f_{h'm'}$, the combinations of $(\nu, f_{h'm'})$ remain the same despite the ordering of the hopping frequencies at hop h . The same conclusion holds by fixing f_{hm} and randomly changing the ordering of the hopping frequencies at hop h' . This is validated by the example given in Tables I and II, where, C1 and C2 in Table I give two orderings of the same hopping frequencies, and, clearly, the overall combination set of $(\nu, f_{h'm'})$ obtained under C1 is identical to that of $(\tilde{\nu}, \tilde{f}_{h'm'})$ under C2. Therefore, we can claim that HFPS does not incur any change to $R(\tau)$ after hopping frequencies are selected by HFCS.

3) *Impact of EPC and RSR on $R(\tau)$* : According to (14) and (25), the joint impact of EPC and RSR is that the phases of radar-transmitted signals are randomly modulated across antennas and hops. As analyzed in [20], PSK modulations can prevent periodic coherent accumulation (which occurs whenever τ is integer times of a hop duration), hence suppressing

periodic sidelobe spikes of R_τ . Given the equivalence between the impact of EPC and RSR on radar signals and that of PSK [20], we conclude that EPC and RSR can suppress periodic sidelobe spikes of $R(\tau)$. A benefit of the suppression is the reduced mutual interference among radar targets. This will be validated in Section VI.

V. NUMERICAL ILLUSTRATION OF THE PROPOSED DESIGN

Having introduced each module in the proposed waveform processing (refer to Fig. 1), we provide a numerical example to demonstrate the overall workflow of incorporating the proposed design in an FH-MIMO DFRC system. For illustration convenience but without loss of generality, small values of parameters are taken: $M = 4$, $K = 5$ and $Q = 1$. The task here is: *transmit symbol $\mathbf{e} = [01\ 0011]^T$ to Bob at hop h .*

1) *Initialization*: According to Section II-D, the number of bits able to be conveyed by HFCS is $E_1 = \lfloor \log_2 C_M^K \rfloor = 2$ and that by HFPS is $E_2 = \lfloor \log_2(M!) \rfloor = 4$. Thus, each radar hop can transmit $E = E_1 + E_2 = 6$ bits. Out of $C_M^K = 5$ different combinations, $2^{E_1} = 4$ combinations are selected as HFCS constellation points and collected by \mathcal{C}_1 . We take \mathcal{C}_1 as

$$\left\{ \begin{array}{l} [\mathcal{C}_1]_0 = \{0, 1, 2, 3\}, [\mathcal{C}_1]_1 = \{0, 1, 2, 4\}, \\ [\mathcal{C}_1]_2 = \{0, 1, 3, 4\}, [\mathcal{C}_1]_3 = \{0, 2, 3, 4\} \end{array} \right\},$$

where $[\mathcal{C}_1]_i$ denotes the i -th constellation point in \mathcal{C}_1 . Out of $M!$ = 16 permutations of hopping frequencies, $2^{E_2} = 16$ permutations are selected as HFPS constellation points and collected by \mathcal{C}_2 , as given by

$$\left\{ \begin{array}{l} [\mathcal{C}_2]_0 = \{3, 2, 1, 0\}, [\mathcal{C}_2]_1 = \{3, 2, 0, 1\}, \\ [\mathcal{C}_2]_2 = \{3, 1, 2, 0\}, [\mathcal{C}_2]_3 = \{3, 1, 0, 2\}, \\ \dots \dots \end{array} \right\}.$$

II) *HFCS and HFPS*: The first $E_1 (= 2)$ bits of \mathbf{e} are used to perform HFCS. Since $(01)_D = 1$, $[\mathcal{C}_1]_1 = \{0, 1, 2, 4\}$ is selected as the set of hopping frequencies, i.e., the zero-th, first, second and fourth sub-bands are used for radar transmission at hop h . Afterwards, $(\cdot)_D$ gives the decimal value of the enclosed bit sequence. Then, the last $E_2 (= 4)$ bits of \mathbf{e} are used for HFPS. Since $(0011)_D = 3$, $[\mathcal{C}_2]_3 = \{3, 1, 0, 2\}$ is selected to pair hopping frequencies with antennas. The first element in $[\mathcal{C}_2]_3$ is 3, which indicates that the 3rd element in $[\mathcal{C}_1]_1$ is used for antenna $m = 0$, i.e., $k_{h0} = 4$. (Here, index starts from 0.) Accordingly, we obtain $\mathbf{k}_h = [4, 1, 0, 2]^T$.

III) *EPC*: Substituting $k_{hm} \forall m$ into (1) gives $s_{hm}(t)$. Then, further substituting $s_{hm}(t)$ and ϕ into (14), the EPC-processed waveform is obtain, i.e., $\tilde{s}_{hm}(t)$.

IV) *RSR*: Initialize the coefficients caused by RSR as $b_{hm} = 1 \forall m$. Given $Q = 1$, a random integer is generated to be the index of RSR antenna. Take $I_0 = 0$ for the index. Enforcing constraint (28), we set $b_{h(I_0+M/2)} = -1$, since $k_{hI_0} > k_{h(I_0+M/2)}$. By multiplying b_{hm} to $\tilde{s}_{hm}(t)$, RSR-processed signal $\check{s}_{hm}(t) = b_{hm}\tilde{s}_{hm}(t)$ is obtained. Then, radar radiates $\check{s}_{hm}(t)$ from antenna m in RF band.

V) *HFCS Decoding at Bob*: The baseband signal received at Bob, i.e., $\check{y}_h(i)$, is shown in Fig. 4. We see that the useful signal is corrupted in noises in the time domain. Taking a 200-point DFT leads to the frequency-domain signal as done in (4),

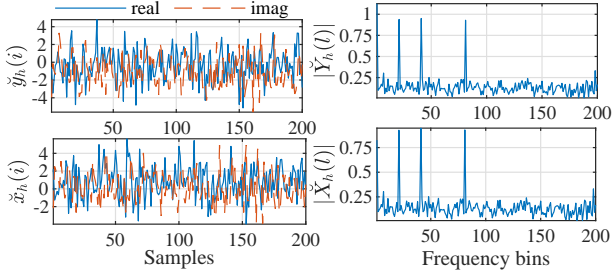


Fig. 4. Signals received by Bob and Eve in time and frequency domains.

we obtain $\check{Y}_h(l)$, whose amplitude is shown in Fig. 4¹. We see four peaks of $|\check{Y}_h(l)|$ and their indexes are $l_0^* = 0$, $l_1^* = 20$, $l_2^* = 40$ and $l_3^* = 80$. Substituting l_m^* into (6), we obtain $\hat{\mathcal{K}}_h = \{0, 1, 2, 4\}$, where \hat{x} denotes an estimate of x . Looking up $\hat{\mathcal{K}}_h$ in \mathcal{C}_1 gives its index in the set which is one in this example. Converting one to E_1 bits, the HFCS sub-symbol is decoded as “01”.

VI) RSR Removal at Bob: Next, we perform Algorithm 2 to remove RSR for Bob. Collecting $\check{Y}_h(l_m^*)$ for $m = 0, 1, \dots, 4$, we obtain $\check{\mathbf{y}}_h = [-0.3416 - 1.0724j, -0.9379 + 0.0325j, 0.9413 - 0.1311j, 0.0198 - 0.9291j]^T$ with AWGNs added. Running Step 2 of Algorithm 2 leads to

$$\check{\mathbf{Y}}_h = \begin{bmatrix} 0 & 1.5764 & 2.5319 & 0.1511 \\ 1.5764 & 0 & 3.5584 & 1.8420 \\ 2.5319 & 2.5584 & 0 & 1.4860 \\ 0.1511 & 1.8420 & 1.4860 & 0 \end{bmatrix}$$

Then Step 3 gives $\mathbf{y}_{\min} = [0.1511, 1.5764, 1.4860, 0.1511]^T$ and $\mathbf{d} = [3, 0, 3, 0]^T$. Sorting \mathbf{y}_{\min} in Step 4 leads to $\mathbf{d}_1 = [0, 3, 2, 1]^T$. This further results in $i = 0$ and $i' = 3$ in Step 6 of Algorithm 2. By comparing l_0/r and l_3/r in Step 7, RSR is detected on $[\check{\mathbf{y}}_h]_0$ and removed by reversing the sign of $[\check{\mathbf{y}}_h]_0$. The output of Algorithm 2 is the RSR-removed signal, i.e., $\tilde{\mathbf{y}}_h = [0.3416 + 1.0724j, -0.9379 + 0.0325j, 0.9413 - 0.1311j, 0.0198 - 0.9291j]^T$.

VII) HFPS Decoding at Bob: With $\tilde{\mathbf{y}}_h$ obtained, Algorithm 1 is performed to decode HFPS sub-symbol. Substituting $\tilde{\mathbf{y}}_h$ in Step 2 gives $\vec{\omega} = [3.0695, -1.4878, 1.5972, 0.1131]^T$. In Step 3, the angles in $\vec{\omega}$ are revised, leading to

$$\vec{\omega} = [-3.2137, -1.4878, -4.6859, -6.1701]^T.$$

Sorting the revised $\vec{\omega}$ gives the index vector $\mathbf{i} = [1, 0, 2, 3]^T$. Comparing $\|e^{-j6.1701} - 1\|_2 = 0.1130$ and $\|e^{-j1.4878} - 1\|_2 = 1.3543$ in Step 5, we know that zigzag has affected $\vec{\omega}$. Thus, \mathbf{i} is circularly shifted once, which gives $\mathbf{i} = [3, 1, 0, 2]^T$. Step 6 constructs \mathbf{P}_h based on \mathbf{i} , as given by

$$\mathbf{P}_h = \begin{bmatrix} 0 & 0 & 1 & 0 \\ 0 & 1 & 0 & 0 \\ 0 & 0 & 0 & 1 \\ 1 & 0 & 0 & 0 \end{bmatrix}.$$

Substituting \mathbf{P}_h in (11), we obtain $\hat{\mathbf{k}}_h = [4, 1, 0, 2]^T$. Looking up $\hat{\mathbf{k}}_h$ in \mathcal{C}_2 gives its index in the set which is three in this

¹Note that the time- and frequency-domain signals received by Eve are also provided in Fig. 4 for comparison. We clearly see four peaks in the frequency spectrum of Eve and the peaks are located at the same discrete frequencies as those of Bob. Thus, Eve detects the same hopping frequencies as Bob.

example. Converting decimal 3 to $E_2 (= 4)$ bits, the HFPS sub-symbol is decoded as “0011”. Both sub-symbols are correctly decoded at Bob applying the proposed methods.

VI. SIMULATION RESULTS

In this section, simulation results are presented to validate the proposed design. Unless otherwise specified, the FH-MIMO radar is configured as: $M = 4$, $Q = \frac{M}{2}$, $K = 20$, $H = 15$, $B = 100$ MHz, $T = 1 \mu\text{s}$ and $L = 200$ (based on the sampling frequency of $2B$); and the communication parameters are: $\phi \sim \mathcal{U}_{[-90^\circ, 90^\circ]}$, $\theta \sim \mathcal{U}_{[-90^\circ, 90^\circ]}$, $\alpha = e^{jx}$ ($x \sim \mathcal{U}_{[0, 2\pi]}$) and $\beta = e^{jy}$ ($y \sim \mathcal{U}_{[0, 2\pi]}$). Here, $\mathcal{U}_{[.,.]}$ stands for the uniform distribution in the subscript region. Throughout simulation, Eve knows the AoD of Bob, if not otherwise specified. The time-domain SNR at Bob is defined based on (3), as given by $\gamma_B = \frac{M|\beta|^2}{\sigma_\xi^2}$, where σ_ξ^2 is the noise power of $\xi(i)$. Based on (9), the decoding SNR at Bob is $L\gamma_B$, where the L times improvement is brought by DFT; see (4). Likewise, the time-domain and decoding SNRs at Eve are given by $\gamma_E = \frac{M|\alpha|^2}{\sigma_z^2}$ and $L\gamma_E$, respectively, where σ_z^2/L is the noise power of $Z(l)$ given in (7). When presenting decoding performance, we use E_b/N_0 , defined as energy per bit to noise power density ratio, i.e.,

$$E_b/N_0 = L\gamma_B BT/E, \quad (30)$$

where E is the number of bits conveyed per radar hop and γ_B can be replaced with γ_E to obtain E_b/N_0 for Eve.

The labels used in the figures are interpreted as follows,

- “Bob-proposed”: indicates that EPC and RSR are performed at radar, and Algorithms 1 and 2 at Bob;
- “Bob-without RSR”: indicates that EPC and Algorithm 1 are performed at radar and Bob, respectively. This is the lower bound of “Bob-proposed” given the absence of RSR removal error caused by running Algorithm 2;
- “Eve”: indicates that EPC and RSR are performed at radar and (18) is solved for HFPS decoding at Eve;
- “Eve-without Bob’s AoD”: is the same as above except the AoD of Bob is unavailable at Eve;
- “Eve-without RSR”: is the same as “Eve” except RSR is not performed at radar. This also acts as a performance indicator of a general HFPS decoding without conducting the proposed EPC and RSR at radar;
- “Bob/Eve-HFCS”: indicates that only HFCS is used for FH-MIMO DFRC, as done in the state of the art [22].

Fig. 5 compares the SERs achieved by Bob and Eve as E_b/N_0 increases. From the curves labeled “Bob-proposed” and “Eve” in Fig. 5, we see that Bob has a decreasing SER against E_b/N_0 and Eve has a close-to-one SER over the same region of E_b/N_0 . This demonstrates the substantially high communication secrecy achieved by the proposed design. Comparing the curves labeled “Bob-proposed” and “HFCS” in Fig. 5, we see the improvement of the proposed scheme over HFCS [22]. In particular, the proposed design reduces SER by more than one order of magnitude at $E_b/N_0 = 23$ dB. This improvement owes to: (i) the use of HFPS which increases the number of bits conveyed per radar hop; (ii) the proposed EPC which solves the AoD-dependent issue of HFPS

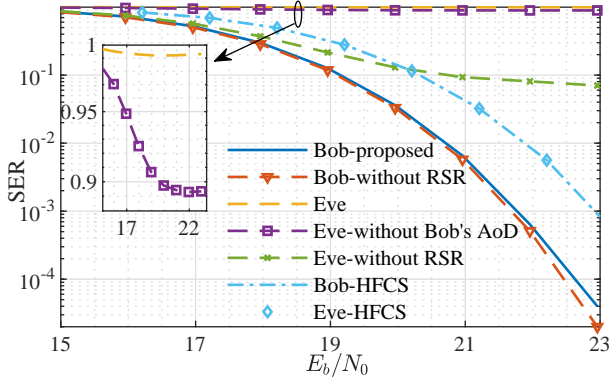


Fig. 5. SER against E_b/N_0 , where γ_B and γ_E are both in $[-10, -2]$ dB. The radar configuration leads to $\lceil \log_2 C_K^M \rceil = 12$ bits conveyed by HFCS sub-symbol and $\lceil \log_2 M! \rceil = 4$ bits by HFPS. Substituting $E = 12 + 4$ into (30) gives the E_b/N_0 region in the figure. The zoomed-in sub-figure helps see the SER of Eve more clearly.

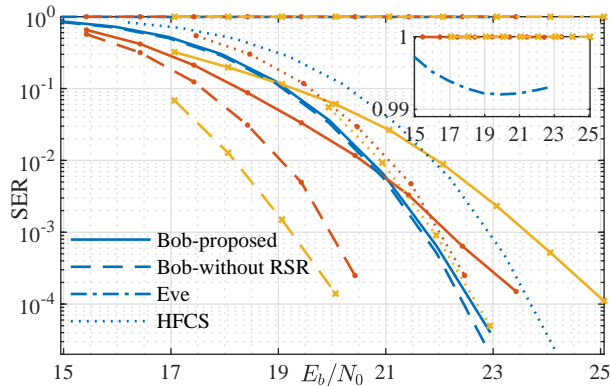


Fig. 6. SER against E_b/N_0 , where $M = 4, 6$ and 8 for curves without markers, with dots and with crosses, respectively, and $Q = \frac{M}{2} \forall M$. $\gamma_B \in [-10, -2]$ dB is set for $M = 4$ and increased by 4 dB and 8 dB for $M = 6$ and 8 , respectively; the same for γ_E . The zoomed-in sub-figure helps see the SER of Eve more clearly.

decoding; see the curves “Bob-proposed” (with EPC) versus “Eve-without RSR” (suffering from the issue); and (iii) the newly designed Algorithm 2 which accurately removes RSR for Bob, c.f., the almost overlapping curves labeled as “Bob-proposed” and “Bob-without RSR”.

We see from Fig. 5 that solely using HFCS leads to identical SER performance of Bob and Eve, which highlights the necessity and significance of our design of enhancing physical layer security. From the three curves related to Eve in Fig. 5, we see three levels of performance degradation at Eve incurred by the proposed design. *First*, by introducing HFPS, the decoding of Eve suffers from an AoD-dependent issue, leading to the convergence of an SER close to 0.1. *Second*, by introducing EPC, the decoding at Eve substantially degrades without the AoD of Eve, increasing the converging SER to about 0.9. *Third*, with RSR performed, the HFPS decoding at Eve is completely incapacitated, incurring SER larger than 0.99 across the whole region of E_b/N_0 .

Fig. 6 compares the SER performance achieved under different values of M . Corresponding to $M = 4, 6$ and 8 , the numbers of bits conveyed by HFPS are 4, 9 and 15, and those by HFCS are 12, 15 and 16, respectively. Comparing the

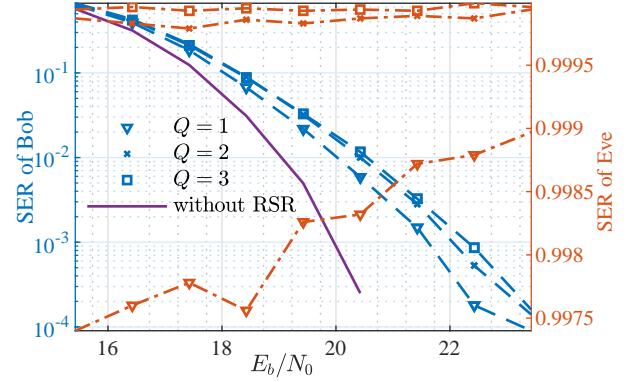


Fig. 7. SER achieved by “Bob-proposed” as E_b/N_0 increases, where $M = 6$, Q takes 1 to 3, the dash-dotted curves use the y -axis on the right, and both γ_B and γ_E are set in $[-6, 2]$ dB.

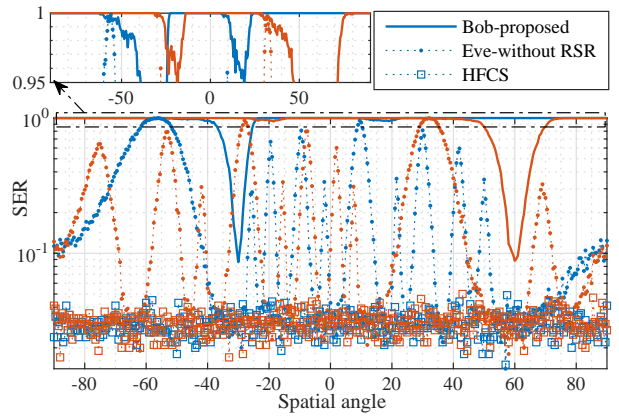


Fig. 8. SER against spatial angle from -90° to 90° with a grid of 0.5° , where $\phi = -30^\circ$ and 60° are observed, $M = 6$, $Q = 3$, and $\gamma_B = -3$ dB.

curves labeled as “Bob-without RSR” and “HFCS”, we see that the increased bits per hop earned by the proposed scheme has the potential of improving SER performance progressively as M increases. We also see from that the gap between the actual SER achieved by our design (“Bob-proposed”) and the bound (“Bob-without RSR”) increases with M , rendering the proposed HFPS plus HFCS slightly worse than the sole HFCS in high E_b/N_0 regions. As expected, this is the price of the substantially high communication secrecy; see the zoomed-in sub-figures. It is noteworthy that, albeit the slight performance loss caused by Algorithm 2, the achievable SER still improves with E_b/N_0 , implying that the loss is compensable. In contrast, the converging SER at Eve is irrecoverable.

Fig. 7 observes the impact of Q on the proposed design. We see that the achievable SER increases negligibly with Q . This validates the robustness of the newly designed Algorithm 2 against Q . We also see that the SER of Eve approaches one tightly even at $Q = 1$ and is closer to one as Q increases. This validates our analysis in Appendix B; specifically, the SER convergence at Eve happens for sure, as the number of permutation matrices leading to error HFPS decoding is larger than one at $Q = 1$ and increases with Q .

Fig. 8 observes the SER performance against the spatial angle. From “Bob-proposed”, we see that the proposed scheme can achieve high secrecy almost omnidirectionally. Except at

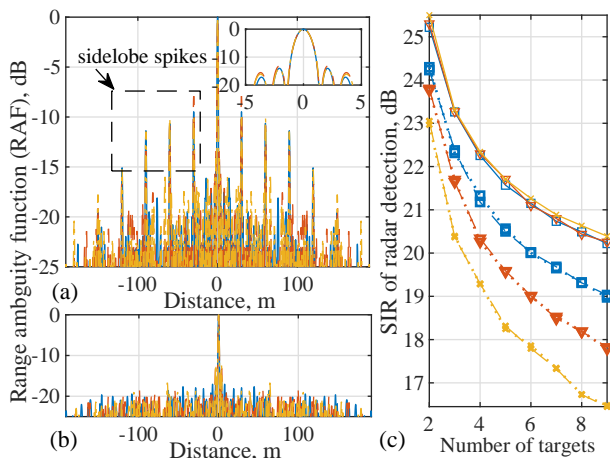


Fig. 9. Impact of the proposed baseband waveform processing on radar detection, where (a) RAFs under three groups of independently and randomly generated hopping frequencies; (b) RAFs after performing HFPS, EPC and RSR on the waveform generated for Fig. 9(a); and (c) SIR against number of targets. Figs. 9(a) and 9(b) take $M = 8$. In 9(c), dotted curves are based on conventional FH-MIMO radar waveform with randomly generated hopping frequencies, dash curves are based on HFCS, and solid curves are based on all the proposed processing; and square, triangle and cross markers correspond to $M = 4, 6$ and 8 , respectively.

the AoD of Bob, the SERs at all the other spatial angles approach one tightly. We also see that the SERs of Bob achieved at different AoDs are similar. This owes to the proposed EPC which removes the AoD-dependence for Bob. From the curve “Eve-without RSR”, we see the reduced physical layer enhancement brought by EPC if the AoD of Bob is known to Eve. Moreover, from the curve “HFCS”, we see that a uniform SER performance is achieved over the whole angular region. This again demonstrates that solely using HFCS for FH-MIMO DFRC is highly prone to eavesdropping.

Last but not least, we illustrate the impact of the proposed waveform processing on FH-MIMO radar performance. Fig. 9(a) is provided to illustrate the impact of HFCS on radar ranging performance. We see that the mainlobes and mainlobe-to-sidelobe ratios (MSRs) under three realizations are almost identical. We also see that the periodicity of sidelobe spikes is the same for different random sets of hopping frequencies. From Fig. 9(b), we see that the proposed waveform processing suppresses the sidelobe spikes, improving the minimum MSR by more than 10 dB. From Fig. 9(c), we see that the improvement on MSR increases SIR of radar detection by up to 4 dB at $M = 8$. We also see that, despite the values of M , the proposed processing leads to similar SIRs. We further see that HFCS waveform achieves the same SIR as the conventional FH-MIMO radar waveform. These observations of Fig. 9 validate our analysis in Section IV-C.

VII. CONCLUSION

In this paper, a secure and high-speed FH-MIMO DFRC system is developed. This is achieved by introducing HFPS constellations to fully exploit information embedding capability embodied in hopping frequencies. This is also accomplished by a new EPC processing which addresses the AoD-dependent issue for Bob and substantially enhances the

physical layer security if the AoD of Bob is unknown to Eve. This is further fulfilled by the proposed RSR which scrambles constellations almost omnidirectionally and forces the SER of Eve, even knowing the AoD of Bob, into converging to one. Validated by simulations, our new design achieves substantially high secrecy, increases data rate and improves SIR of radar detection. As a future work, we will introduce multi-antenna receiver for Bob and develop new methods to further improve decoding performance.

APPENDIX

A. Calculation of (4)

Based on (3), the L -point DFT of the signal component in $y_h(i)$, denoted by $Y_h^s(l)$, can be calculated as

$$\begin{aligned} Y_h^s(l) &= \beta \sum_{m=0}^{M-1} e^{-jmu\phi} \frac{1}{L} \sum_{i=0}^{L-1} e^{j2\pi r i k_{hm}/L} e^{-j\frac{2\pi l i}{L}} \\ &= \beta \sum_{m=0}^{M-1} e^{-jmu\phi} \frac{\sin\left(\pi L \left(\frac{l-rk_{hm}}{L}\right)\right)}{L \sin\left(\pi \left(\frac{l-rk_{hm}}{L}\right)\right)} e^{-j2\pi \frac{L-1}{2} \left(\frac{l-rk_{hm}}{L}\right)}. \end{aligned}$$

From the above result, we see that $\sin\left(\pi L \left(\frac{l-rk_{hm}}{L}\right)\right)$ is always zero due to the integer r ; see (2). This indicates that $Y_h^s(l)$ is only non-zero when the denominator equals to zero, i.e., $\sin\left(\pi \left(\frac{l-rk_{hm}}{L}\right)\right) = 0$. The sine function only takes zero provided $\left(\frac{rk_{hm}+l}{L}\right)$ is an integer which leads to $l = rk_{hm}$. From the above analysis, $Y_h^s(l)$ only takes non-zero values at $l = rk_{hm}$. Using the Dirac function, $Y_h^s(l)$ is written as in (4).

B. Proof of Proposition 1

We first illustrate that $f_b^{\Re}(\mathbf{P})$ conforms to a normal distribution. Denote $\mathbf{P}^T \mathbf{P}_h$ in (22) as $\check{\mathbf{P}}$ and rewrite $f_b^{\Re}(\mathbf{P})$ as

$$f_b^{\Re}(\mathbf{P}) = \Re \left\{ \mathbf{a}_{\theta\phi}^H (\check{\mathbf{P}} \mathbf{b}_h \odot \check{\mathbf{P}} \mathbf{a}_{\theta\phi}) \right\} = \Re \left\{ \sum_{m=0}^{M-1} \check{b}_{hm} e^{j\Delta_{hm}} \right\},$$

where $\check{b}_{hm} = [\check{\mathbf{P}} \mathbf{b}_h]_m$ and Δ_{hm} is the difference between the phases of $[\mathbf{a}_{\theta\phi}]_m$ and $[\check{\mathbf{P}} \mathbf{a}_{\theta\phi}]_m$, i.e.,

$$\Delta_{hm} = m(2\pi/M + u_{\theta\phi}) - \arg \left\{ [\check{\mathbf{P}} \mathbf{a}_{\theta\phi}]_m \right\} \quad \forall m, \quad (31)$$

where $\mathbf{a}_{\theta\phi}$ is given in (18) and $u_{\theta\phi} = u_{\theta} - u_{\phi}$. Based on (20), we have

$$\mathbb{P}\{\check{b}_{hm} = 1\} = (M-Q)/M; \quad \mathbb{P}\{\check{b}_{hm} = -1\} = Q/M. \quad (32)$$

As \check{b}_{hm} ($m = 0, 1, \dots, M-1$) are independent Bernoulli-like variables, a weighted sum of them with constant-modulus weights, i.e., $\sum_{m=0}^{M-1} \check{b}_{hm} e^{j\Delta_{hm}}$, approaches to a normally distributed variable according to the central limit theorem [27]. As the real part of a complex normal variable, $f_b^{\Re}(\mathbf{P})$ also conforms to a normal distribution, i.e., $f_b^{\Re}(\mathbf{P}) \sim \mathcal{N}(\mu_f, \sigma_f^2)$.

We proceed to calculate the parameters of $f_b^{\Re}(\mathbf{P})$. Taking the expectation of $f_b^{\Re}(\mathbf{P})$ leads to

$$\mu_f = \mathbb{E} \left\{ f_b^{\Re}(\mathbf{P}) \right\} = \Re \left\{ \underbrace{\sum_{m=0}^{M-1} \mathbb{E} \left\{ \check{b}_{hm} \right\}}_{\mu_{f1}} \underbrace{\mathbb{E} \left\{ e^{j\Delta_{hm}} \right\}}_{\mu_{f2}} \right\}, \quad (33)$$

where the randomness in $e^{j\Delta_{hm}}$ is caused by $\check{\mathbf{P}}$; see (31). Based on (32), we can calculate μ_{f1} as

$$\mu_{f1} = \left(1 \times \frac{M-Q}{M} + (-1) \times \frac{Q}{M} \right) = \frac{M-2Q}{M}. \quad (34)$$

Given a large sample set of $\check{\mathbf{P}}$, the second term on the RHS of (31) has a uniformly distributed angle, i.e.,

$$\mathbb{P} \left\{ \arg \left\{ [\check{\mathbf{P}}\mathbf{a}_{\theta\phi}]_m \right\} = m' \left(u_{\theta\phi} + \frac{2\pi}{M} \right) \right\} = \frac{1}{M} \quad \forall m' \leq M-1.$$

Based on the above PDF and (31), μ_{f2} can be calculated as

$$\begin{aligned} \mu_{f2} &= e^{jm \left(u_{\theta\phi} + \frac{2\pi}{M} \right)} \left(\sum_{m'=0}^{M-1} \frac{e^{-jm' \left(u_{\theta\phi} + \frac{2\pi}{M} \right)}}{M} \right) \quad (35) \\ &= e^{jm \left(u_{\theta\phi} + \frac{2\pi}{M} \right)} \times \frac{e^{-j\frac{M-1}{2} \left(u_{\theta\phi} + \frac{2\pi}{M} \right)} \sin \left(\frac{M \left(u_{\theta\phi} + \frac{2\pi}{M} \right)}{2} \right)}{M \sin \left(\frac{\left(u_{\theta\phi} + \frac{2\pi}{M} \right)}{2} \right)}. \end{aligned}$$

Substituting (34) and (35) into (33) and after some manipulations, we obtain

$$\mu_f = \Re \left\{ \frac{M-2Q}{M^2} \frac{\sin^2 \left(\frac{M \left(u_{\theta\phi} + \frac{2\pi}{M} \right)}{2} \right)}{\sin^2 \left(\frac{\left(u_{\theta\phi} + \frac{2\pi}{M} \right)}{2} \right)} \right\}, \quad (36)$$

which leads to (24).

Next, we calculate the variance of $f_b^{\Re}(\mathbf{P})$. Given that the variance of the real part of a complex Gaussian-distributed variable is half the full variance, we calculate σ_f^2 as in (37), where $\stackrel{(a)}{=}$ is achieved based on two facts. First, the expectations of products between different \check{b}_{hm} are zero due to their mutual independence. Second, $\mathbb{E} \left\{ \sum_{m=0}^{M-1} \check{b}_{hm} e^{-j\Delta_{hm}} \right\} = \mu_f$ is plugged in, since $\mathbb{E} \left\{ \sum_{m=0}^{M-1} \check{b}_{hm} e^{-j\Delta_{hm}} \right\}$, calculated within the curly brackets in (36), is already a real value.

We proceed to investigate the impact of the normally distributed $f_b^{\Re}(\mathbf{P})$ on HFPS decoding at Eve. Referring to (18), an error HFPS decoding happens at Eve when solving (18) returns a \mathbf{P} satisfying the following event

$$\mathcal{E} : f_b^{\Re}(\mathbf{P}) > f_b^{\Re}(\mathbf{P}_h) = (M-2Q) \quad \forall \mathbf{P} \neq \mathbf{P}_h. \quad (38)$$

Therefore, to prove that RSR causes the convergence of SER of Eve to one, we turn to validating there is always \mathbf{P} making event (38) happen.

Given the normal distribution $f_b^{\Re}(\mathbf{P}) \sim \mathcal{N}(\mu_f, \sigma_f^2)$, the probability of event \mathcal{E} can be expressed using the complementary error function, i.e.,

$$\mathbb{P}\{\mathcal{E}\} = \frac{\text{erfc} \{h(\mu_f, Q)\}}{2}, \text{ s.t. } h(\mu_f, Q) = \frac{(M-2Q) - \mu_f}{\sqrt{M - \mu_f^2}},$$

where σ_f given in (24) has been plugged in. As illustrated in Appendix C, $h(\mu_f, Q)$ is a non-increasing function of $\mu_f \in [0, M-2Q]$. In addition, it can be readily validated that $h(\mu_f, Q)$ is also a decreasing function of Q . Therefore, given the decreasing monotonicity of $\text{erfc}\{\cdot\}$ against its argument,

$\mathbb{P}\{\mathcal{E}\}$ is maximized by taking $\mu_f = 0$ and $Q = 1$. This gives $\mathbb{P}\{\mathcal{E}\} \geq \frac{1}{2} \text{erfc} \left\{ \frac{(M-2)}{\sqrt{M}} \right\}$. Then the number of \mathbf{P} making \mathcal{E} happen, denoted by $N_{\mathbf{P}}$, satisfies

$$N_{\mathbf{P}} = \mathbb{P}\{\mathcal{E}\} \times M! \geq \frac{M!}{2} \text{erfc} \left\{ \frac{(M-2)}{\sqrt{M}} \right\}, \quad (39)$$

where $M!$ is the number of all possible permutation matrices in \mathcal{P}_{Eve} ; see (18). As shown in Fig. 10, $N_{\mathbf{P}}$ is a non-decreasing function of M and the lower bound of $N_{\mathbf{P}}$ is one at the minimum $M = 2$. This confirms the existence of \mathbf{P} causing (38) for any values of $M (\geq 2)$ and hence the convergence of the SER to one at Eve.

Before concluding the proof, we explain the angular region confinement in (23). From (37), we see that to ensure a non-negative variance, $M - \mu_f^2 \geq 0$ is required. By plugging (36) in the inequality, a region of $u_{\theta\phi}$ can be obtained. Unfortunately, analytical expression for the region is unavailable, due to the discrete sinc function in (36). Nevertheless, it can be inferred that $u_{\theta\phi}$ leading to $M - \mu_f^2 < 0$ can only be located in the mainlobe of the sinc function in (36). This is because μ_f^2 is upper bounded by $\frac{16(M-2Q)^2}{81\pi^4}$ in the sidelobe regions², i.e., $0 \leq u_{\theta\phi} \leq \frac{2\pi(M-2)}{M}$. For tractability, we use this region in Proposition 1, even though the actual region is slightly larger, as shown in Fig. 3.

C. Monotonicity of $h(\mu_f, Q)$

Taking the first partial derivative of $h(\mu_f, Q)$ against μ_f , after lengthy yet straightforward manipulations, leads to

$$\frac{\partial h(\mu_f, Q)}{\partial \mu_f} = \frac{\mu_f(M-2Q) - M}{(M - \mu_f^2)^{\frac{3}{2}}}.$$

As σ_f^2 given in (37) is non-negative, we have $M \geq \mu_f^2$. Based on (36), we have $\mu_f \leq (M-2Q)$. Thus, the numerator of the above first partial derivative is non-positive. That is, $h(\mu_f, Q)$ is a non-increasing function of μ_f .

REFERENCES

- [1] J. Choi *et al.*, "Millimeter-wave vehicular communication to support massive automotive sensing," *IEEE Commun. Mag.*, vol. 54, no. 12, pp. 160–167, 2016.
- [2] J. A. Zhang, X. Huang, Y. J. Guo, J. Yuan, and R. W. Heath, "Multibeam for joint communication and radar sensing using steerable analog antenna arrays," *IEEE Trans. Veh. Technol.*, vol. 68, no. 1, pp. 671–685, Jan 2019.
- [3] B. Paul, A. R. Chiriyath, and D. W. Bliss, "Survey of RF communications and sensing convergence research," *IEEE Access*, vol. 5, pp. 252–270, 2017.
- [4] C. Sturm and W. Wiesbeck, "Waveform design and signal processing aspects for fusion of wireless communications and radar sensing," *Proc. IEEE*, vol. 99, no. 7, pp. 1236–1259, July 2011.
- [5] F. Liu, L. Zhou, C. Masouros, A. Li, W. Luo, and A. Petropulu, "Toward dual-functional radar-communication systems: Optimal waveform design," *IEEE Trans. Signal Process.*, vol. 66, no. 16, pp. 4264–4279, Aug 2018.
- [6] X. Yuan, Z. Feng, J. A. Zhang, W. Ni, R. P. Liu, Z. Wei, and C. Xu, "Waveform optimization for MIMO joint communication and radio sensing systems with training overhead," *arXiv preprint arXiv:2002.00338*, 2020.

²This is calculated by substituting $u_{\theta\phi} = \frac{\pi}{M}$ into the sinc function in (36), since the peak of the first sidelobe is approximately achieved at the angle.

$$\begin{aligned} \sigma_f^2 &= \frac{1}{2} \text{var} \left\{ \sum_{m=0}^{M-1} \check{b}_{hm} e^{-j\Delta_{hm}} \right\} = \frac{1}{2} \left\{ \mathbb{E} \left\{ \left(\sum_{m=0}^{M-1} \check{b}_{hm} e^{-j\Delta_{hm}} \right)^2 \right\} - \left(\mathbb{E} \left\{ \sum_{m=0}^{M-1} \check{b}_{hm} e^{-j\Delta_{hm}} \right\} \right)^2 \right\} \\ &\stackrel{(a)}{=} \frac{1}{2} \times \left(\left(\sum_{m=0}^{M-1} 1^2 \times \frac{M-Q}{M} + (-1)^2 \times \frac{Q}{M} \right) - \mu_f^2 \right) = \frac{1}{2} \times (M - \mu_f^2) \end{aligned} \quad (37)$$

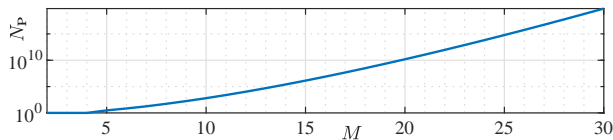


Fig. 10. Non-decreasing lower bound of N_P derived in (39) against M .

- [7] S. C. Surender and R. M. Narayanan, "UWB noise-OFDM netted radar: Physical layer design and analysis," *IEEE Trans. Aerosp. Electron. Syst.*, vol. 47, no. 2, pp. 1380–1400, 2011.
- [8] P. Kumari, J. Choi, N. Gonzalez-Prelcic, and R. W. Heath, "IEEE 802.11ad-based radar: An approach to joint vehicular communication-radar system," *IEEE Trans. Veh. Technol.*, vol. 67, no. 4, pp. 3012–3027, April 2018.
- [9] G. R. Muns, K. V. Mishra, C. B. Guerra, Y. C. Eldar, and K. R. Chowdhury, "Beam alignment and tracking for autonomous vehicular communication using IEEE 802.11 ad-based radar," in *IEEE INFOCOM 2019-IEEE Conference on Computer Communications Workshops (INFOCOM WKSHPs)*. IEEE, 2019, pp. 535–540.
- [10] P. Kumari, S. A. Vorobyov, and R. W. Heath, "Adaptive virtual waveform design for millimeter-wave joint communication-radar," *IEEE Trans. Signal Process.*, pp. 1–1, 2019.
- [11] M. L. Rahman, J. A. Zhang, X. Huang, Y. J. Guo, and R. W. Heath Jr, "Framework for a perceptive mobile network using joint communication and radar sensing," *IEEE Trans. Aerosp. Electron. Syst.*, 2019.
- [12] J. Moghaddasi and K. Wu, "Multifunctional transceiver for future radar sensing and radio communicating data-fusion platform," *IEEE Access*, vol. 4, pp. 818–838, 2016.
- [13] A. Hassanien, M. G. Amin, Y. D. Zhang, and F. Ahmad, "Signaling strategies for dual-function radar communications: An overview," *IEEE Aerosp. Electron. Syst. Mag.*, vol. 31, no. 10, pp. 36–45, 2016.
- [14] L. Zheng, M. Lops, Y. C. Eldar, and X. Wang, "Radar and communication coexistence: An overview: A review of recent methods," *IEEE Signal Processing Magazine*, vol. 36, no. 5, pp. 85–99, 2019.
- [15] A. Hassanien, M. G. Amin, Y. D. Zhang, and F. Ahmad, "Dual-function radar-communications: Information embedding using sidelobe control and waveform diversity," *IEEE Trans. Signal Process.*, vol. 64, no. 8, pp. 2168–2181, April 2016.
- [16] X. Wang, A. Hassanien, and M. G. Amin, "Dual-function MIMO radar communications system design via sparse array optimization," *IEEE Trans. Aerosp. Electron. Syst.*, vol. 55, no. 3, pp. 1213–1226, June 2019.
- [17] A. Hassanien, E. Aboutanios, M. G. Amin, and G. A. Fabrizio, "A dual-function MIMO radar-communication system via waveform permutation," *Digit. Signal Process.*, vol. 83, pp. 118–128, 2018.
- [18] T. W. Tedesso and R. Romero, "Code shift keying based joint radar and communications for EMCON applications," *Digit. Signal Process.*, vol. 80, pp. 48–56, 2018.
- [19] A. Hassanien, M. G. Amin, E. Aboutanios, and B. Himed, "Dual-function radar communication systems: A solution to the spectrum congestion problem," *IEEE Signal Process. Mag.*, vol. 36, no. 5, pp. 115–126, Sep. 2019.
- [20] I. P. Eedara, A. Hassanien, M. G. Amin, and B. D. Rigling, "Ambiguity function analysis for dual-function radar communications using PSK signaling," in *2018 52nd Asilomar Conf. on Signals, Syst., and Computers*, Oct 2018, pp. 900–904.
- [21] I. P. Eedara, M. G. Amin, and A. Hassanien, "Analysis of communication symbol embedding in FH MIMO radar platforms," in *2019 IEEE Radar Conf. (RadarConf)*, April 2019, pp. 1–6.
- [22] W. Baxter, E. Aboutanios, and A. Hassanien, "Dual-function MIMO radar-communications via frequency-hopping code selection," in *2018 52nd Asilomar Conf. on Signals, Syst., and Computers*, Oct 2018, pp. 1126–1130.
- [23] F. Gini, A. De Maio, and L. Patton, *Waveform design and diversity for advanced radar systems*. Institution of engineering and technology London, 2012.
- [24] K. Wu, W. Ni, J. A. Zhang, R. P. Liu, and J. Guo, "Secrecy rate analysis for millimeter-wave lens antenna array transmission," *IEEE Commun. Lett.*, vol. 24, no. 2, pp. 272–276, 2020.
- [25] C. Chen and P. P. Vaidyanathan, "MIMO radar ambiguity properties and optimization using frequency-hopping waveforms," *IEEE Trans. Signal Process.*, vol. 56, no. 12, pp. 5926–5936, Dec 2008.
- [26] K. Wu, W. Ni, T. Su, R. P. Liu, and Y. J. Guo, "Robust unambiguous estimation of angle-of-arrival in hybrid array with localized analog subarrays," *IEEE Trans. Wireless Commun.*, vol. 17, no. 5, pp. 2987–3002, May 2018.
- [27] M. E. Eltayeb, J. Choi, T. Y. Al-Naffouri, and R. W. Heath, "Enhancing secrecy with multiantenna transmission in millimeter wave vehicular communication systems," *IEEE Trans. Veh. Technol.*, vol. 66, no. 9, pp. 8139–8151, 2017.